Seismic response of tunnel near fault fracture zone under incident SV waves

Zhongxian Liu [a,*], Jiaqiao Liu [a], Qiang Pei [b], Haitao Yu [c], Chengcheng Li [a], Chengqing Wu [d,*]

[a] *Tianjin Key Laboratory of Soft Soil Properties and Engineering Environment, Tianjin Chengjian University, Tianjin 300384, China*
[b] *Research & Development Center of Civil Engineering Technology, Dalian University, Dalian 116622, China*
[c] *Key Laboratory of Geotechnical and Underground Engineering of Ministry of Education, Tongji University, Shanghai 200092, China*
[d] *School of Civil and Environmental Engineering, University of Technology Sydney, NSW, Australia*

Abstract

This study investigated the impact of a non-causative fault on the dynamic response of a nearby lined tunnel under the incidence of plane SV waves using the indirect boundary element method. The effects of several critical parameters, such as the incident frequency, the inclination degree of the fault, the distance between the fault and the tunnel on the hoop stress of the lined inner and outer walls, were explored intensively. The numerical results indicated that the non-causative fault could significantly change the hoop stress distribution of inner and outer surfaces of the tunnels. In general, for the vertically incident seismic waves, when the tunnel was located in the foot wall (under the fault), the hoop stress within the tunnel was significantly greater than that of the tunnels in the non-fault half space, with an amplification factor of up to 117%. The amplification effect became more pronounced as the fault dip angle increased. However, when the tunnel was located in the hanging wall (above the fault), the non-causative fault could produce a significant shielding effect on the dynamic response of the tunnel under high frequency wave incidence, with the reduction of hoop stress being up to 81%. For low-frequency waves, though, the fault could lead to an increase of the hoop stress of the tunnel of up to 152%. The research results will provide a reference for the seismic design and safety protection of underground structures in non-causative fault sites.

Keywords: Non-causative fault; Indirect boundary element method; Fault fracture zone; Lined tunnel

1 Introduction

In recent years, large-scale infrastructure construction has been promoted in many cities around the world. Lined tunnels are widely used in road and railway engineering. The high-intensity seismic zone has a great number of underground lined tunnels, such as the Sichuan–Tibet line in China. A large amount of earthquake disaster investigations has shown that underground structures can suffer severe damage during strong earthquakes, such as the Osaka–Kobe Earthquake in 1995, the Taiwan Chi-Chi Earthquake (Wang et al., 2001), and the Wenchuan Earthquake (Li, 2008). Therefore, it is of great practical engineering significance to study the seismic responses and seismic performances in underground lined tunnels.

The seismic response rule of lined tunnels has been thoroughly studied by many researchers in recent years. The seismic analysis of lined tunnels includes analytical methods and numerical methods. For analytical methods, wave function expansion methods have been widely used to solve the scattering of seismic waves for a tunnel, such as the solutions for incident SH waves (Gao et al., 2017; Lee & Trifunac, 1979; Liang et al., 2010) or for P, SV, and

---

Rayleigh waves (Liang et al., 2004; Liu & Wang, 2012; Yu et al., 2018).

However, more efficient numerical methods should be developed for practical complex models because analytical methods are usually limited to simple computational models and ideal seismic inputs. These methods include the finite element method (FEM) (Lin et al., 2016; Shahrour et al., 2010; Yu et al., 2017; Zhang & Liu, 2020), finite difference method (FDM) (Cai, 2008; Manolis et al., 2015; Pitilakis et al., 2014), spectral element method (Gharti et al., 2012; Lambrecht & Friederich, 2010), and boundary element method (BEM) (Alielahi & Adampira, 2018; Rodriguez-Castellanos et al., 2006).

Compared with FEM and FDM, BEM has certain advantages among the different methods. The calculation dimension of the problem is simplified, the infinite radiation condition can be accurately satisfied without introducing artificial boundaries, and high-frequency numerical dispersion is avoided. Therefore, BEM has also been widely used in the dynamic analysis of underground structures. Stamos and Beskos (1996) numerically calculated the dynamic response of tunnels buried in viscoelastic or elastic half space to a body wave and a surface wave via a direct boundary element method. Parvanova et al. (2014) simulated the seismic response of several tunnels in a half space. Panji and Ansari (2017) used BEM to research the scattering of transient SH waves by the lined tunnels. Alielahi et al. (2015) used BEM to amplify an unlined tunnel with SV and P waves incident vertically. Liu et al. (2017) used IBIEM to solve the scattering of plane P1 waves with a shallow lined tunnel in a poroelastic half space.

It is worth noting that the previous research was mainly focused on the tunnel model of a general site, while the seismic response of a tunnel in a non-causative fault zone has rarely been studied. In practice, for a complex local site, a non-causative fault may have a serious impact on the ground motion of earthquakes due to the multiple reflections of waves in a fault fracture zone (Karabulut & Bouchon, 2007; Li et al., 2012; Wang et al., 2014), in turn affecting the seismic response of a lined tunnel near a fault site. Furthermore, since the lined tunnels are close to a non-causative fault fracture zone, the seismic dynamics is also influenced by the fracture in the rock mass (Fan et al., 2018, 2020; Zhou et al., 2017). Therefore, the seismic response analysis of a non-causative fault fracture zone has gradually caught attention in the arena of engineering.

However, in the line selection design of a tunnel, it is inevitable that a tunnel will be close to a non-causative fault fracture zone. So far, few studies have been conducted on the seismic dynamic interaction between a non-causative fault fracture zone and a lined tunnel. Lin et al. (2006) investigated the influence of a large blind thrust slip on the safety of lined tunnels. Cividini et al. (2010) studied the extension of the fault in an alluvial sediment where the tunnel is located and its influence on the permanent lining. Wang et al. (2012) analyzed the seismic damage of a cross-fault tunnel under various loads. Ardeshiri-Lajimi et al. (2015) explored the influence of a large underground cavern and the fault distribution in the seismic design. Huang et al. (2017) solved the nonlinear dynamic responses of a circular lining tunnel near normal fault in half space under the action of oblique incident P waves via FEM.

For a fault-lined tunnel model, research into the scattering of SV waves via a non-causative fault–tunnel system has rarely been published in the literature due to the complexity of researching into the coupling effect of plane waves.

In this study, the indirect boundary element method (IBEM) was used to study the seismic response of a lined tunnel near a non-causative fault site for the incidence of plane SV waves. Using the proposed IBEM, the diffracted wave field within the lined tunnel and the surrounding soil can be accurately calculated in wideband frequency domain. Because the discretization of the boundary is merely necessary, the pre-processing is relatively simple and friendly. The advantage is that the numerical dispersion does not appear in the high-frequency and broadband scattering. In this paper, the effects of important factors such as the angle of the fault, the horizontal distance between the fault and the lined tunnel as well as the frequency and angle of the incident wave on the dynamic interaction between the fault fracture zone and the lined tunnel were investigated in detail. The dynamic stress concentration factors (DSCFs) for the outer and inner surfaces of lined tunnel were presented in this study. Finally, several important conclusions were obtained, which were conducive to the anti-seismic design of lined tunnels near the non-causative fault site.
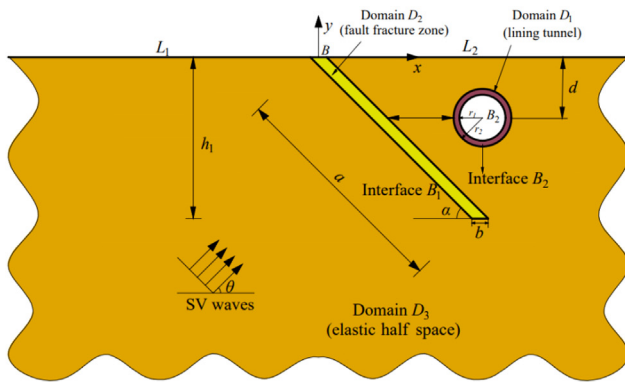
2 Numerical model

As shown in Fig. 1, there was a non-causative fault and an infinitely long circular-lined tunnel in the elastic half space. The long circular tunnel was shallowly buried in the bedrock half space with depth d. The inner and outer radius of the lined tunnel were r_1 and r_2. D_1, D_2, and D_3 denoted the domains of the half space, fault fracture zone, and lined tunnel, respectively. The interface between regions D_1 and D_2 was B_1, and the interface between regions D_1 and D_3 was B_2. Other symbols and descriptions were summarized in Table 1. The domains of the half space, fault, and tunnel were assumed to be elastic, isotropic, and homogenous, respectively. The incidences of the plane SV waves were considered from the bottom half space, and the problem to be solved was the two-dimensional scattering of SV waves by the lined tunnel near a fault site.

3 Calculation method for the seismic response in a tunnel-fault system

In this research, the IBEM was used to simulate the fluctuation of the bedrock half space, the fault fracture zone, and the lined cavity. The basic principle of the IBEM
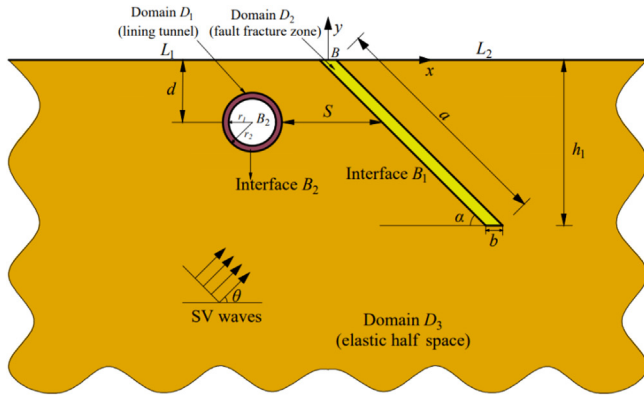
(a) the tunnel in the foot wall of a near-fault site (model 1)

(b) the tunnel in the hanging wall of a near-fault site (model 2)

Fig. 1. Numerical model for the tunnel-fault system under seismic waves.

was based on the single-layer potential theory, which discretized a boundary with a certain number of elements and applies virtual loads to a boundary to obtain the scattered wave field. As depicted in Fig. 2, the virtual wave sources were applied directly to the boundary to construct a scattered wave field, which was a direct implementation of the Huygens principle.

According to the continuous displacement and stress conditions at the interface B_1, B_2, the zero-stress conditions on the half space surface, fault fracture zone surface and

inner wall of the tunnel, the virtual wave source density was solved. The scattering field of each part was obtained, and finally, the total elastic wave field could be determined by adding together the free field and the scattering field. The proposed method was applicable to tunnels of any shape. In order to facilitate the analysis, a circular lined tunnel was taken as an example in this research.

3.1 Wave field analysis

The wave field in the half space could be divided into a free field and a scattered field.

3.1.1 Scattered wave field analysis of the bedrock half space

The total displacement field and the stress field of the elastic half space D_1 could be expressed as follows:

$$u_m^{(t,1)}(x) = u_m^{(f,1)}(x) + u_m^{(s,1)}(x), x \in D_1, \quad (1)$$

$$\sigma_m^{(t,1)}(x) = \sigma_m^{(f,1)}(x) + \sigma_m^{(s,1)}(x), x \in D_1, \quad (2)$$

where $u_m^{(f,1)}$ and $\sigma_m^{(f,1)}$ represented the m-direction displacement and stress of the free field under the incident elastic wave, and $u_m^{(s,1)}$ and $\sigma_m^{(s,1)}$ represented the m-direction displacement and stress of the scattering field, respectively. It could be determined from the single-layer potential theory that the corresponding displacement and stress in the scattering field could be expressed as follows:

$$u_m^{(s,1)}(x) = \int_{s_1} \varphi_j^{(s,1)}(y_1) G_{mj}^{(s,1)}(x, y_1) \mathrm{d}S_{y_1}, \quad (3)$$

$$\sigma_m^{(s,1)}(x) = -0.5\varphi_j^{(s,1)}(x) + \int_{s_1} \varphi_j^{(s,1)}(y_1) T_{mj}^{(s,1)}(x, y_1) \mathrm{d}S_{y_1}, \quad (4)$$

where $x \in D_1, y_1 \in S_1$. $S_1 = \{L_1 \cup B_1 \cup L_2 \cup B_2\}$ was the discrete element surface on the half space as shown in Fig. 2. $\varphi_j^{(s,1)}(y_1)$ was the virtual load density at the position y_1 applied on the boundary S_1. $G_{mj}^{(s,1)}(x, y_1)$ and $T_{mj}^{(s,1)}(x, y_1)$ were the displacement and stress Green's functions of the bedrock half space, respectively, which referred to the m-direction stress and displacement of the position x by unit force vector j acting on the position y_1.

Table 1
List of some important symbols.

Symbol	Description	Symbol	Description
d	The depth to the tunnel center	S	The horizontal distances between the tunnel and the fault
r_1, r_2	The inner and outer radius of the lined tunnel	a	The length of fault
ζ	Damping ratio	b	The width of fault
D_1, D_2, D_3	Domain of the half space, the fault fracture zone and the tunnel	h_1	The vertical height of fault
v_1, v_2, v_3	Poisson's ratio of D_1, D_2 and D_3	B_1	The interface between regions D_1 and D_2
μ_1, μ_2, μ_3	Shear modulus of D_1, D_2 and D_3	B_2	The interface between regions D_1 and D_3
ρ_1, ρ_2, ρ_3	Density of D_1, D_2 and D_3	B_3	The inner wall of the lined tunnel
$c_{\beta1}, c_{\beta2}, c_{\beta3}$	SV waves velocity in D_1, D_2 and D_3	B	Surface of fault fracture zone
α	The fault dip	f	Actual frequency
θ	Incident angle of SV waves	L_1, L_2	Half space surface

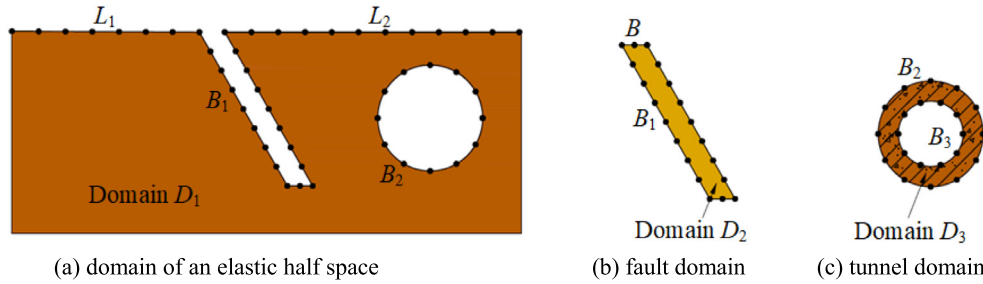(a) domain of an elastic half space   (b) fault domain   (c) tunnel domain

Fig. 2. Domain division of the tunnel-fault system and boundary discrete elements.

3.1.2 Scattered wave field analysis of the fault fracture zone

The scattering displacement and the stress of the fault fracture zone D_2 could be expressed as follows:

$$u_m^{(s,2)}(x) = \int_{S_2} \varphi_j^{(s,2)}(y_2) G_{mj}^{(s,2)}(x, y_2) \mathrm{d}S_{y_2}, \tag{5}$$

$$\sigma_m^{(s,2)}(x) = -0.5\varphi_j^{(s,2)}(x) + \int_{S_2} \varphi_j^{(s,2)}(y_2) T_{mj}^{(s,2)}(x, y_2) \mathrm{d}S_{y_2}, \tag{6}$$

where $x \in D_2$, $y_2 \in S_2$, $S_2 = \{B_1 \cup B\}$ was the discrete element surface on the fault fracture zone as shown in Fig. 2. $\varphi_j^{(s,2)}(y_2)$ was the virtual load density at the position y_2 applied on the boundary S_2. $G_{mj}^{(s,2)}(x, y_2)$ and $T_{mj}^{(s,2)}(x, y_2)$ were the displacement and stress Green's functions of the fault fracture zone, respectively. It should be noted that there was no free field in domain D_2 of the fault fracture zone, and the scattering field was considered the total wave field.

3.1.3 Scattered wave field analysis of the lined tunnel

The scattering displacement and stress of the lined tunnel D_3 could be expressed as follows:

$$u_m^{(s,3)}(x) = \int_{S_3} \varphi_j^{(s,3)}(y_3) G_{mj}^{(s,3)}(x, y_3) \mathrm{d}S_{y_3}, \tag{7}$$

$$\sigma_m^{(s,3)}(x) = -0.5\varphi_j^{(s,3)}(x) + \int_{S_3} \varphi_j^{(s,3)}(y_3) T_{mj}^{(s,3)}(x, y_3) \mathrm{d}S_{y_3}, \tag{8}$$

applied on the boundary S_3. $G_{mj}^{(s,3)}(x, y_3)$ and $T_{mj}^{(s,3)}(x, y_3)$ were the displacement and stress Green's functions of the lined tunnel, respectively. It should be noted that there was no free field in domain D_3 of the lined tunnel, and the scattering field was considered the total wave field.

3.2 Boundary conditions and solutions

According to the continuous condition based on the displacement and stress of the boundary, the virtual load density could be solved by establishing the equations of each part of the wave field, which were obtained as described in the previous section of the paper. The boundary conditions could be expressed as follows:

$$\begin{cases} u_m^{(t,1)}(x) = u_m^{(s,2)}(x), x \in B_1, \\ \sigma_m^{(t,1)}(x) = \sigma_m^{(s,2)}(x), x \in B_1, \\ u_m^{(t,2)}(x) = u_m^{(s,3)}(x), x \in B_2, \\ \sigma_m^{(t,2)}(x) = \sigma_m^{(s,3)}(x), x \in B_2, \\ \sigma_m^{(t,1)}(x) = 0, x \in \{L_1 \cup L_2\}, \\ \sigma_m^{(s,2)}(x) = 0, x \in B, \\ \sigma_m^{(s,3)}(x) = 0, x \in B_3. \end{cases} \tag{9}$$

According to Eqs. (1)–(9), Eq. (10) was obtained:

$$\begin{cases} \int_{S_1} \varphi_j^{(s,1)}(y_1) G_{mj}^{(s,1)}(x, y_1) dS_{y_1} - \int_{S_2} \varphi_j^{(s,2)}(y_2) G_{mj}^{(s,2)}(x, y_2) dS_{y_2} = -u_m^{(f,1)}(x), x \in B_1, \\ -0.5\left[\varphi_j^{(s,1)}(x) + \varphi_j^{(s,2)}(x)\right] + \int_{S_1} \varphi_j^{(s,1)}(y_1) T_{mj}^{(s,1)}(x, y_1) \mathrm{d}S_{y_1} - \int_{S_2} \varphi_j^{(s,2)}(y_2) T_{mj}^{(s,2)}(x, y_2) \mathrm{d}S_{y_2} = -\sigma_m^{(f,1)}(x), x \in B_1, \\ \int_{S_1} \varphi_j^{(s,1)}(y_1) G_{mj}^{(s,1)}(x, y_1) dS_{y_1} - \int_{S_3} \varphi_j^{(s,3)}(y_3) G_{mj}^{(s,3)}(x, y_3) dS_{y_3} = -u_m^{(f,1)}(x), x \in B_2, \\ -0.5\left[\varphi_j^{(s,1)}(x) + \varphi_j^{(s,3)}(x)\right] + \int_{S_1} \varphi_j^{(s,1)}(y_1) T_{mj}^{(s,1)}(x, y_1) \mathrm{d}S_{y_1} - \int_{S_3} \varphi_j^{(s,3)}(y_3) T_{mj}^{(s,3)}(x, y_3) \mathrm{d}S_{y_3} = -\sigma_m^{(f,1)}(x), x \in B_2, \\ -0.5\varphi_j^{(s,1)}(x) + \int_{S_1} \varphi_j^{(s,1)}(y_1) T_{mj}^{(s,1)}(x, y_1) \mathrm{d}S_{y_1} = -\sigma_m^{(f,1)}(x), x \in \{L_1 \cup L_2\}, \\ -0.5\varphi_j^{(s,2)}(x) + \int_{S_2} \varphi_j^{(s,2)}(y_2) T_{mj}^{(s,2)}(x, y_2) \mathrm{d}S_{y_2} = 0, x \in B, \\ -0.5\varphi_j^{(s,3)}(x) + \int_{S_3} \varphi_j^{(s,3)}(y_3) T_{mj}^{(s,3)}(x, y_3) \mathrm{d}S_{y_3} = 0, x \in B_3, \end{cases} \tag{10}$$

where $x \in D_3$, $y_3 \in S_3$, $S_3 = \{B_2 \cup B_3\}$ was the discrete element surface on the lined tunnel as shown in Fig. 2. $\varphi_j^{(s,3)}(y_3)$ was the virtual load density at the position y_3

where superscripts 1, 2 and 3 represented the partial wave sources of the bedrock half space, fault fracture zone and the lined tunnel, respectively, and Green's functions that

were used were full space Green's functions. Assuming that $\phi_j(y)$ was constant for each element, there was a set of linear equations:

$$F_1 = \frac{\Delta S}{(\lambda + 2\mu)} \times \left\{ 1 + \frac{2i}{\pi\left[1 - \gamma - \lg\left(h \times \frac{\Delta S}{4}\right)\right]} \right\} + \frac{\Delta S}{\mu}$$

$$\times \left\{ 1 + \frac{2i}{\pi\left[1 - \gamma - \lg\left(k \times \frac{\Delta S}{4}\right)\right]} \right\}, \quad (14)$$

$$\begin{cases} \sum_{l_1=1}^{N_1} \varphi_j^{(s,1)}(y_{1,l_1}) g_{mj}^{(s,1)}(x_{n_1}, y_{1,l_1}) - \sum_{l_2=1}^{N_2} \varphi_j^{(s,2)}(y_{2,l_2}) g_{mj}^{(s,2)}(x_{n_2}, y_{2,l_2}) = -u_m^{(f,1)}(x_{n_1}), \\ -0.5\left[\varphi_j^{(s,1)}(x_{n_1}) + \varphi_j^{(s,2)}(x_{n_1})\right] + \sum_{l_1=1}^{N_1} \varphi_j^{(s,1)}(y_{1,l_1}) t_{mj}^{(s,1)}(x_{n_1}, y_{1,l_1}) - \sum_{l_2=1}^{N_2} \varphi_j^{(s,2)}(y_{2,l_2}) t_{mj}^{(s,2)}(x_{n_2}, y_{2,l_2}) = -\sigma_m^{(f,1)}(x_{n_1}), \\ \sum_{l_1=1}^{N_1} \varphi_j^{(s,1)}(y_{1,l_1}) g_{mj}^{(s,1)}(x_{n_2}, y_{1,l_1}) - \sum_{l_3=1}^{N_3} \varphi_j^{(s,3)}(y_{3,l_3}) g_{mj}^{(s,3)}(x_{n_2}, y_{3,l_3}) = -u_m^{(f,1)}(x_{n_2}), \\ -0.5\left[\varphi_j^{(s,1)}(x_{n_2}) + \varphi_j^{(s,3)}(x_{n_2})\right] + \sum_{l_1=1}^{N_1} \varphi_j^{(s,1)}(y_{1,l_1}) t_{mj}^{(s,1)}(x_{n_2}, y_{1,l_1}) - \sum_{l_3=1}^{N_3} \varphi_j^{(s,3)}(y_{3,l_3}) t_{mj}^{(s,3)}(x_{n_2}, y_{3,l_3}) = -\sigma_m^{(f,1)}(x_{n_2}), \\ -0.5\varphi_j^{(s,1)}(x_{n_3}) + \sum_{l_1=1}^{N_1} \varphi_j^{(s,1)}(y_{1,l_1}) t_{mj}^{(s,1)}(x_{n_3}, y_{1,l_1}) = -\sigma_m^{(f,1)}(x_{n_3}), \\ -0.5\varphi_j^{(s,2)}(x_{n_4}) + \sum_{l_2=1}^{N_2} \varphi_j^{(s,2)}(y_{2,l_2}) t_{mj}^{(s,2)}(x_{n_4}, y_{2,l_2}) = 0, \\ -0.5\varphi_j^{(s,3)}(x_{n_5}) + \sum_{l_3=1}^{N_3} \varphi_j^{(s,3)}(y_{3,l_3}) t_{mj}^{(s,3)}(x_{n_5}, y_{3,l_3}) = 0, \end{cases} \quad (11)$$

$$g_{mj}(x,y) = \int_{y-\frac{\Delta S}{2}}^{y+\frac{\Delta S}{2}} G_{mj}(x,y) dS_y, \quad t_{mj}(x,y)$$

$$= \int_{y-\frac{\Delta S}{2}}^{y+\frac{\Delta S}{2}} T_{mj}(x,y) dS_y, \quad (12)$$

where ΔS was the unit length; N_1, N_2, and N_3 were the number of discrete elements of the elastic bedrock half space boundary surface, the fault fracture zone boundary surface, and the lined tunnel boundary surface, respectively. Additionally, $x_{n_1} \in B_1$, $x_{n_2} \in B_2$, $x_{n_3} \in \{L_1 \cup L_2\}$, $x_{n_4} \in B$, $x_{n_5} \in B_3$, $y_{1,l_1} \in S_1$, $y_{2,l_2} \in S_2$, and $y_{3,l_3} \in S_3$. n_1, n_2, n_3, n_4, n_5, l_1, l_2, l_3 represented the numbering of the corresponding boundary discrete element, respectively. $x \neq y$, Eqs. (11) and (12) were used to calculate directly. When $x = y$, the expansion of Green's function was needed for use to solve the analytic integral:

$$g_{mj}(x,y) = \frac{i}{8}(F_1 + F_2)\delta_{mj}, \quad t_{mj}(x,y) = \frac{1}{2}\delta_{mj}, \quad (13)$$

$$F_2 = \frac{h^2 \times \Delta S^3}{8(\lambda + 2\mu)}$$

$$\times \left\{ \frac{1}{12} + \frac{i}{2\pi} \times \left[\frac{1}{9} - \frac{\gamma}{3} - \frac{\lg(h \times \Delta S/4)}{3}\right] \right\}$$

$$- \frac{k^2 \times \Delta S^3}{8\mu}$$

$$\times \left\{ \frac{1}{12} + \frac{i}{2\pi} \times \left[\frac{1}{9} - \frac{\gamma}{3} - \frac{\lg\left(k \times \frac{\Delta S}{4}\right)}{3}\right] \right\}, \quad (15)$$

where δ_{mj} was the Delta function; λ and μ were the Lame constants; h and k were the compressional and shear wave numbers, respectively; and γ was the Euler constant, which was taken as 0.5772.

The equation was established according to the above boundary conditions, and the virtual load density of each element was obtained. The scattering wave field was obtained by multiplying Green's function and the virtual load density. The total wave field inside the fault fracture zone and the lined tunnel was the scattering field. The total

(a) vertical displacement
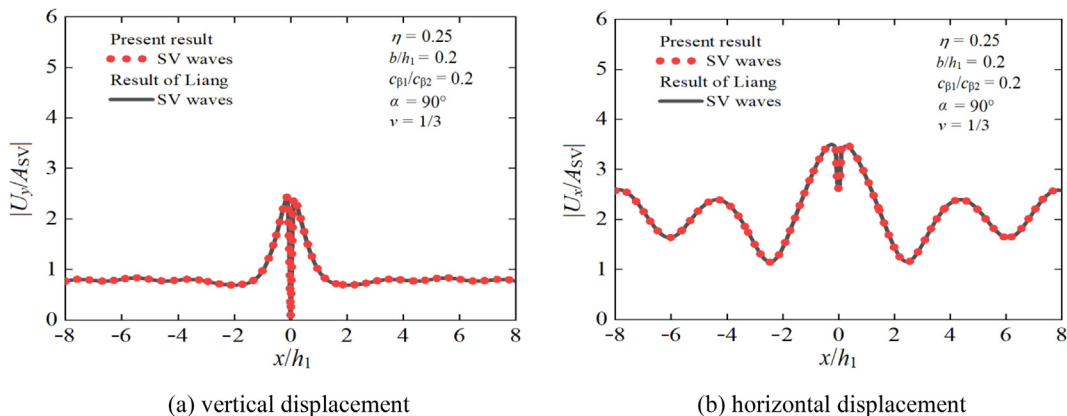
(b) horizontal displacement

Fig. 3. Comparison of the results of this model for the surface displacement of the fault with the results of Liang et al. (2009) for vertically incident SV waves.

wave field in the bedrock half space was the sum of the scattered field and the free field. The feature of this method was that the virtual loads were directly applied to the boundary, which was a direct realization of the Huygens principle.

4 Accuracy verification

As the study on the lined tunnel in the near-fault site had no result to compare, the model of the fault-lined tunnel was degraded into a single fault (the material parameters inside and outside the tunnel were equal).

Figure 3 shows the displacement amplitudes of the ground surface compared with the results reported by Liang et al. (2009) using the IBEM for vertically incident SV waves. To degenerate the solution to a single fault case, the calculated parameters were set as follows: damping ratio $\zeta = 0.001$, mass density $\rho_1/\rho_2/\rho_3 = 1.0/1.0/1.0$, SV wave velocity $c_{\beta 1}/c_{\beta 2}/c_{\beta 3} = 5.0/1.0/5.0$, Poisson's ratio $v_1 = v_2 = v_3 = 1/3$, the length of half space surface $L_1 = L_2 = 8000$ m, the length of fault $a = 1000$ m, ratio of the width to the depth of the fault fracture zone $b/h_1 = 0.2$, dip of the fault $\alpha = 90°$, incident angle of SV waves of 90°, and non-dimensional frequency $\eta = 0.25$ (the influence of the tunnel on the seismic response could be ignored). The horizontal and vertical displacement amplitudes (U_x, U_y) in the figures have been normalized by the incident wave displacement amplitude A_{SV}. It was shown that the degenerated results provided via the proposed method agreed well with the results from the literature.

5 Numerical analysis

As shown in Fig. 1, a circular tunnel was shallowly buried in the near-fault site. The inner radius was $r_1 = 5$ m, the outer radius was $r_2 = (10/9)r_1 = 5.56$ m, and the depth $d = 15$ m. The fault fracture zone width was $b = 50$ m, the length was $a = 1000$ m, and the fault was categorized as a narrow fault. The other calculated parameters were set as follows: Poisson's ratio $v_1 = v_2 = v_3 = 0.25$, mass density $\rho_1 = 2000$ kg/m^3, $\rho_2 = 1800$ kg/m^3, $\rho_3 = 2500$ kg/m^3, SV wave velocity $c_{\beta 1} = 1200$ m/s^2, $c_{\beta 2} = 240$ m/s^2, and $c_{\beta 3} = 2400$ m/s^2 (rigid lining). The damping ratio $\zeta = 0.01$.

5.1 DSCFs for the inner and outer surfaces of the single-lining tunnel

Figures 4–9 ploted the DSCFs for vertically incident SV waves, $\sigma_{\theta\theta}' = |\sigma_{\theta\theta}/\sigma_0| = |\sigma_{\theta\theta}/\mu_1 k_1^2|$, $\sigma_{\theta\theta}$ is the hoop stress of the lined tunnel, $\sigma_\theta = \mu_1 k_1^2$ was the amplitude of incident wave stress in half space; μ_1 and k_1 were the shear modulus and the shear wave velocity of the half space, respectively. The fault dip angles $\alpha = 30°$, 45°, and 60°, the horizontal distances between the tunnel and the fault of $S = 20$, 50, and 100 m and the actual frequencies of the incident elastic wave were $f = 5.0$, 10.0, and 20.0 Hz, respectively.

Generally, when the lined tunnel was located at the lower wall of the fault fracture zone, the existence of the fault caused the DSCFs of the lined tunnel to have an amplification effect. When the tunnel was located at upper
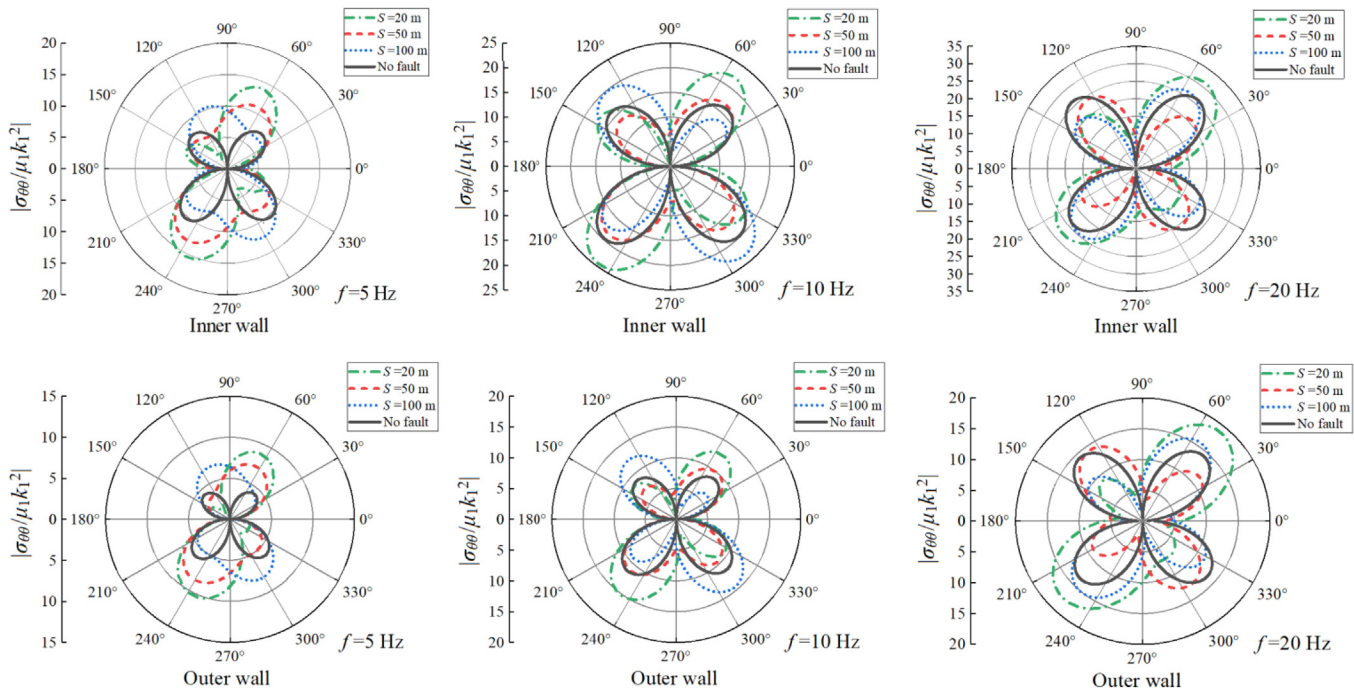

Fig.4. DSCFs of the inner and outer surfaces of the lined tunnel at different distances between the tunnel and the fault for SV wave incidence ($\alpha = 30°$) (model 1).
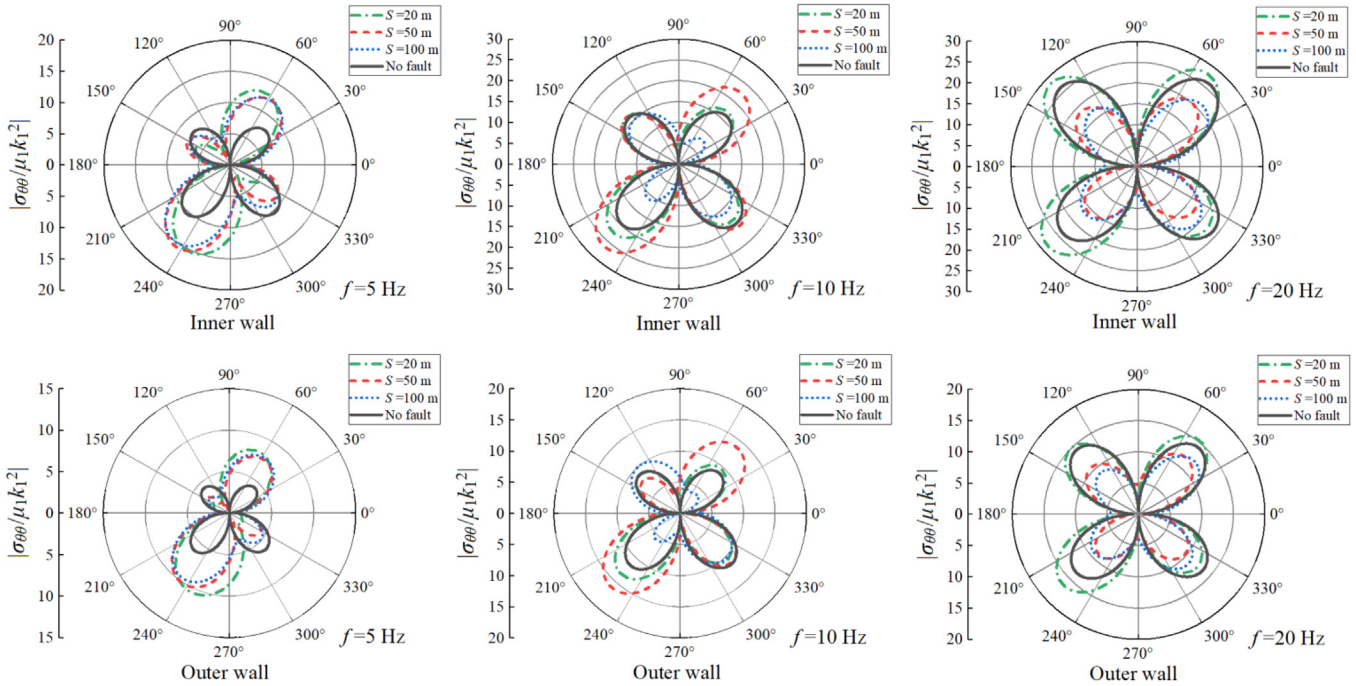
Fig. 5. DSCFs of the inner and outer surfaces of the lined tunnel at different distances between the tunnel and the fault for SV wave incidence ($\alpha = 45°$) (model 1).
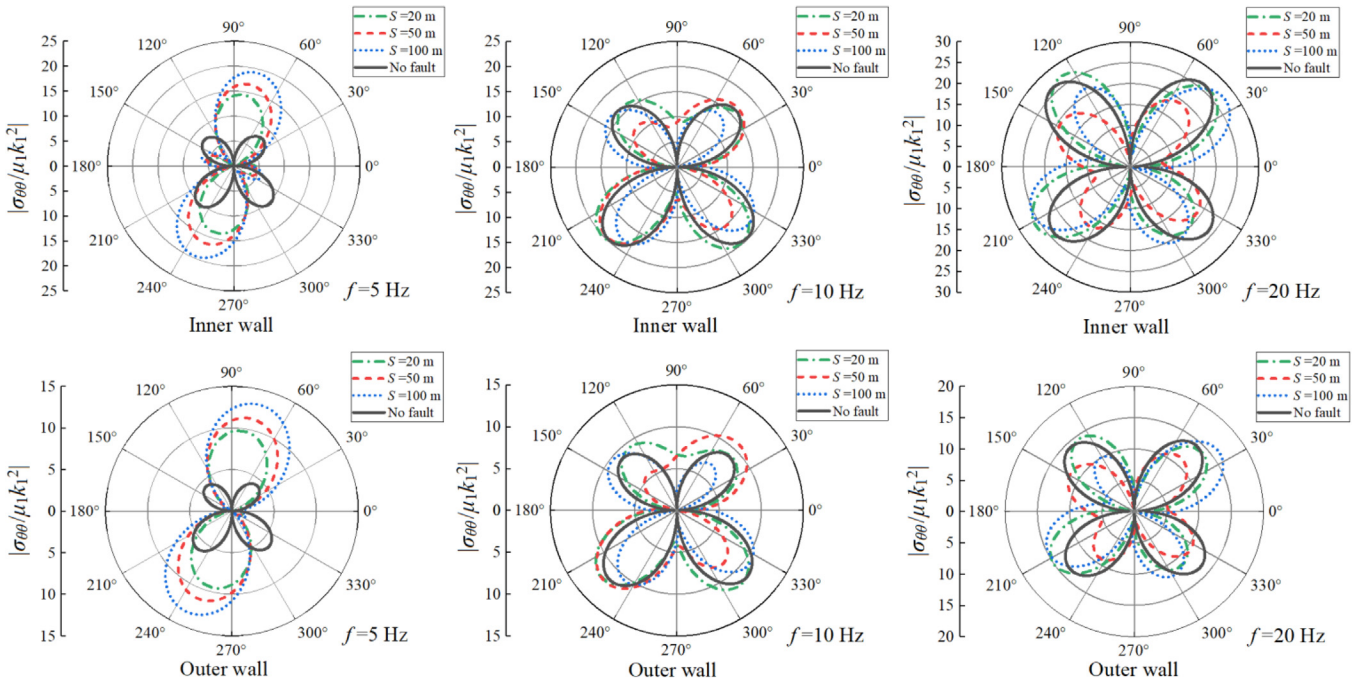

Fig. 6. DSCFs of the inner and outer surfaces of the lined tunnel at different distances between the tunnel and the fault for SV wave incidence ($\alpha = 60°$) (model 1).

wall of the fault, the DSCFs of the inner and outer surfaces of the lined tunnel decreased.

5.1.1 The tunnel in the foot wall of a near-fault site (model 1)

The general rule could be determined from the comparison of the inner and outer wall stresses. The inner wall stress was greater than the outer wall stress, and the stress curve characteristics for the inner and outer wall were similar. The existence of the fault fracture zone had a certain amplification effect on the inner and outer wall stresses when the lined tunnel was in the foot wall of the fault fracture zone.

With the increase of the fault dip angle, the DSCF amplification effect of the lined tunnel increased gradually. For the case of $S = 50$ m, $f = 5$ Hz, $\alpha = 30°$, $45°$, and $60°$,
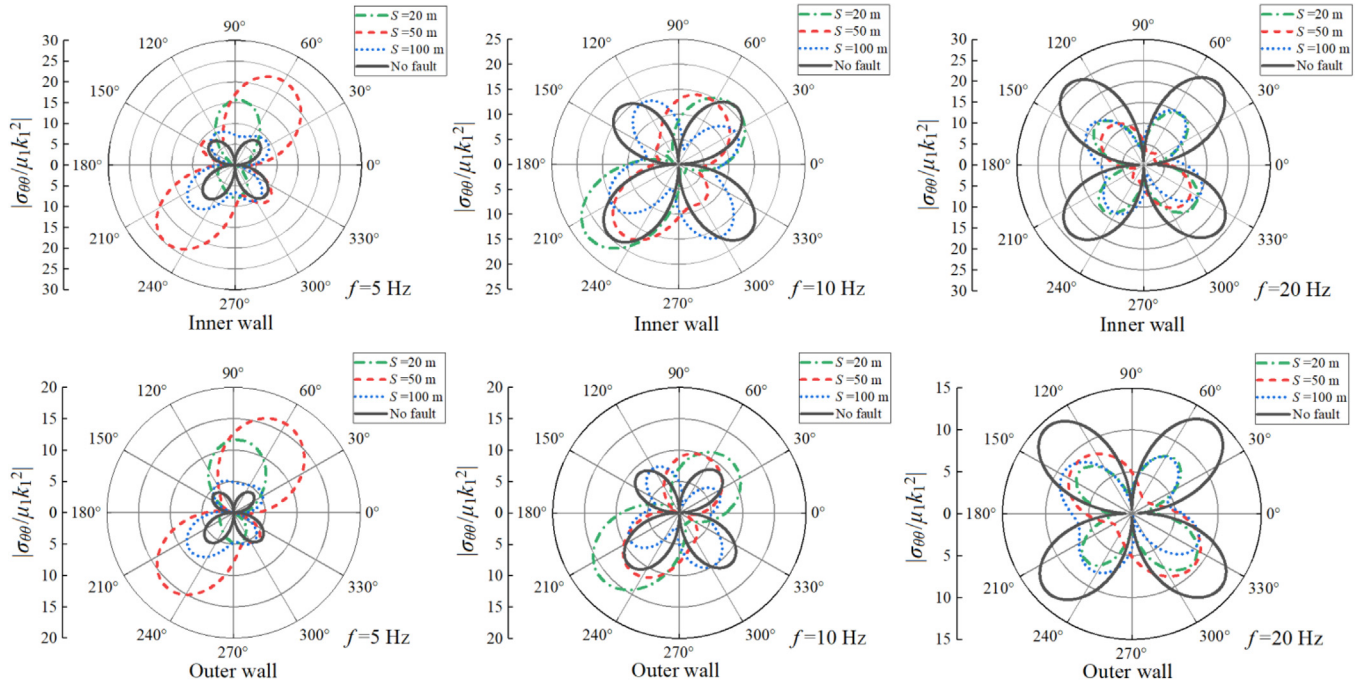
Fig. 7. DSCFs of the inner and outer surfaces of the lined tunnel at different distances between the tunnel and the fault for SV wave incidence ($\alpha = 30°$) (model 2).
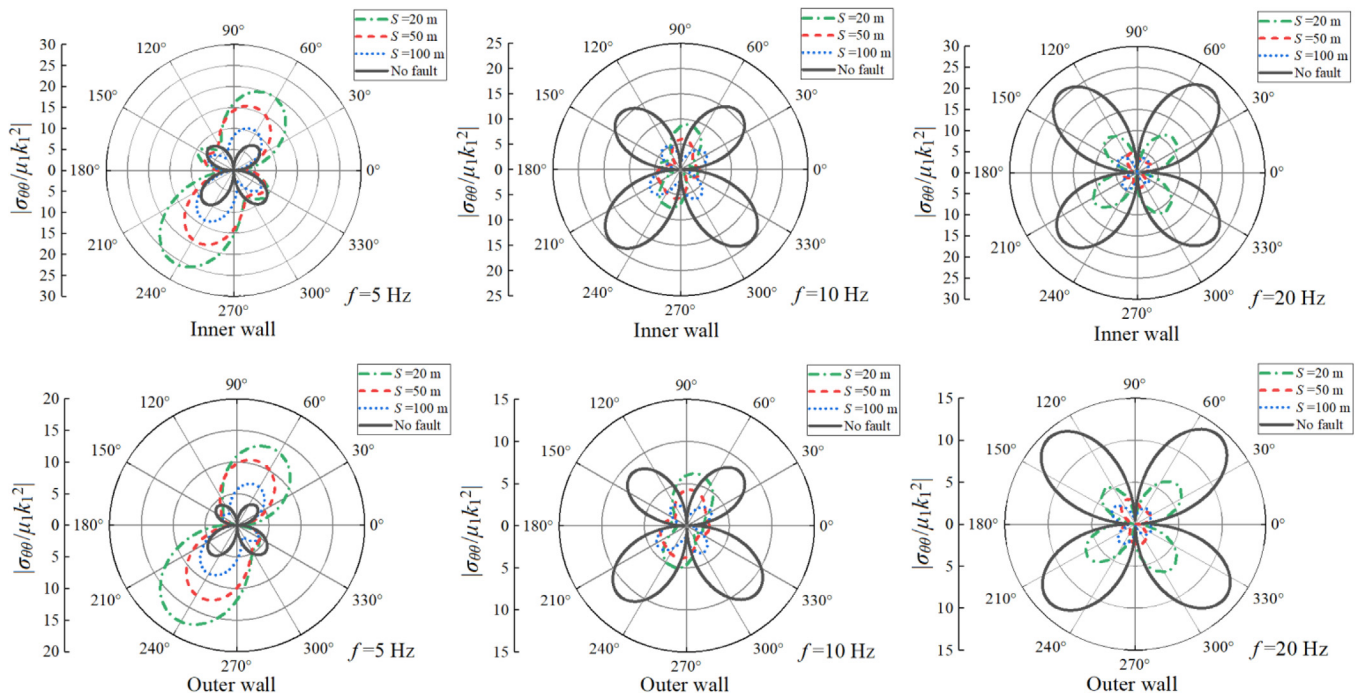

Fig. 8. DSCFs of the inner and outer surfaces of the lined tunnel at different distances between the tunnel and the fault for SV wave incidence ($\alpha = 45°$) (model 2).

compared with the no fault case, the maximum DSCFs increased 26%, 51%, and 60% at the inner wall of the lined tunnel, respectively, as can be observed from Figs. 4–6.

When $\alpha = 60°$, the fault fracture zone had a great influence on the tunnel, and the DSCF amplification at the outer wall reached 117%. From the view of engineering, more
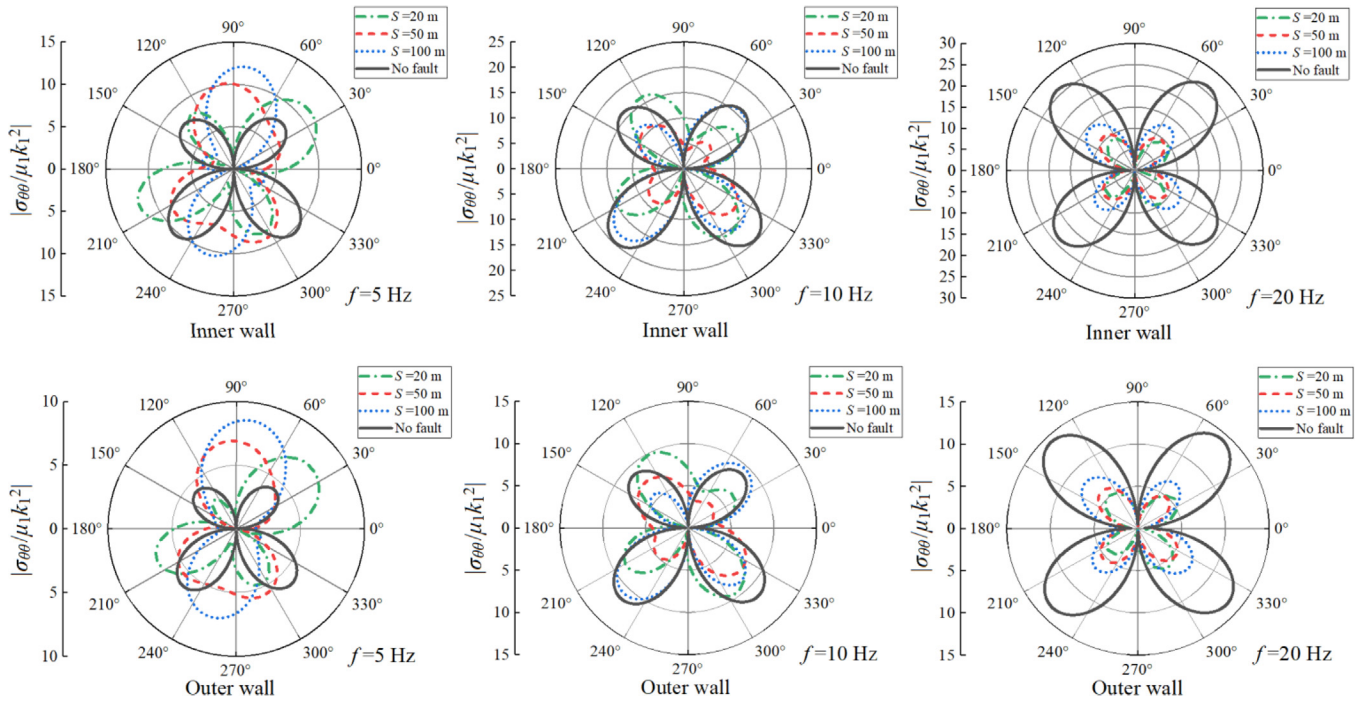
Fig. 9. DSCFs of the inner and outer surfaces of the lined tunnel at different distances between the tunnel and the fault for SV wave incidence ($\alpha = 60°$) (model 2).

attention should be paid to the seismic design of the tunnel near the fault fracture zone with large dip angle.

The amplification effect was more significant at low frequency. For $\alpha = 30°$, $S = 20$ m, $f = 5$, 10, and 20 Hz, the DSCFs at the inner wall reached 15.50, 24.47 and 31.28, increasing by 49%, 24% and 19%, respectively, compared with the no-fault cases (10.39, 19.76 and 26.21).

For fault fracture zones with different dip angles, the influences of horizontal distance S on DSCF were different. When the SV wave was incident, $\alpha = 30°$, with the decrease of the horizontal distance S between the tunnel and the fault, the DSCF amplification effect of the lined tunnel became more and more serious. As offered in Fig. 4, $\alpha = 30°$, $f = 5$ Hz, $S = 20$, 50, and 100 m, compared with the no fault case, the peak of the DSCFs at the inner wall were 49%, 26%, and 19%, respectively.

5.1.2 The tunnel in the hanging wall of a near-fault site (model 2)

When the lined tunnel was in the hanging wall of the fault fracture zone, the inner and outer wall DSCFs were amplified at low frequency and shielded at high frequency. Due to the multiple scattering and interface effect of SV waves between the surfaces of the fault fracture zone and the tunnel, the response characteristic was more complicated. The shielding effect was more pronounced with the increase of frequency. As illustrated in Fig. 8, $\alpha = 45°$, $f = 5$ Hz, the DSCF amplification effect still existed. The amplification effect decreased with the increase of distance S. For example, $\alpha = 45°$, $f = 5$ Hz, $S = 20$, 50, and 100 m, compared with the no fault case, the maximum DSCF

amplification ratios at the inner wall of the lined tunnel were 152%, 85%, and 42%, respectively. When $f = 10$ Hz and 20 Hz, the shielding effect appeared significantly. For the case of $S = 20$ m, $f = 10$ Hz and 20 Hz, the shielding effect of inner wall reached 69% and 81%, respectively.

With the increase of the fault dip angle, the DSCF shielding effect of the lined tunnel increased gradually. It can be found from Figs. 7–9 that for the case of $S = 20$ m, $f = 20$ Hz, and for $\alpha = 30°$, 45°, and 60°, compared with the no fault case, the maximum DSCF amplitudes decreased 41%, 53%, and 62% at the inner wall of the lined tunnel, respectively.

5.2 Stress and displacement cloud diagrams of the lining tunnel

For a lined tunnel near the fault region, the cloud diagram of DSCF for models 1 and 2 for incident SV waves were given in Fig. 10. In addition, horizontal and vertical displacement cloud diagrams of the lined tunnel were depicted in Figs. 11 and 12 respectively. The distance between the fault and the lined tunnel was $S = 50$ m, the dip angle of the fault was $\alpha = 45°$, and seismic waves were vertically incident. The displacement amplitude in the figures has been normalized by the incident wave displacement amplitude, and the tunnel size has been normalized by the tunnel outer wall radius r_2.

In Fig. 10, the inner wall stresses were greater than the outer wall stresses. The stress concentrations on the left and right sides of the lined tunnel as well as the arch shoulders and arch feet were obvious, while the stress factors on

(a) no fault

(b) the lined tunnel in the foot wall ($\alpha = 45°$)

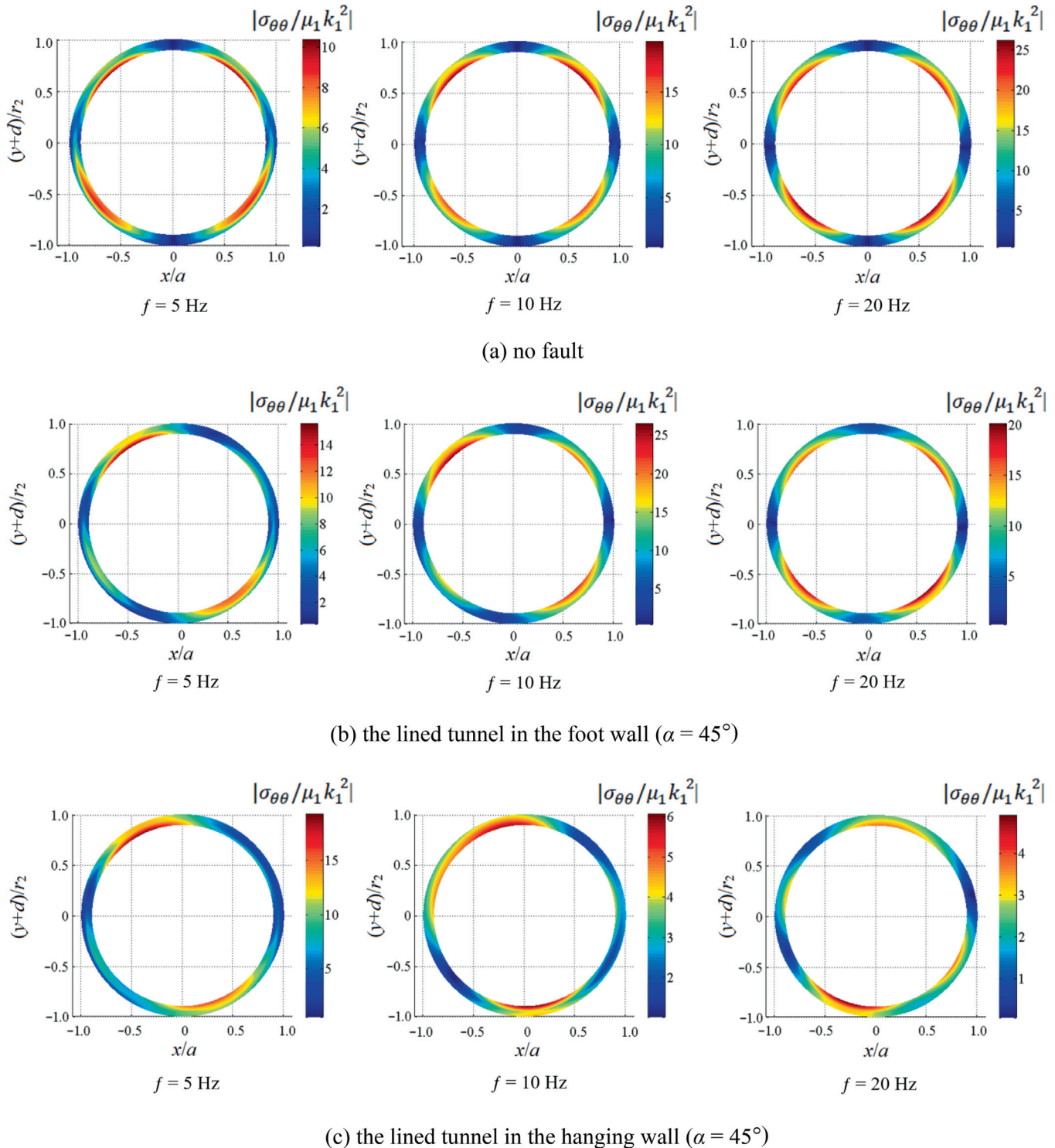(c) the lined tunnel in the hanging wall ($\alpha = 45°$)

Fig. 10. Circumferential stress cloud diagrams of the lined tunnel in a near fault site.

the top and bottom of the lined tunnel were smaller. The incident wave frequency had an important influence on the wave scattering. When the tunnel was in the foot wall of the fault fracture zone, the influence on the stress amplitude and spatial distribution characteristics of the lined tunnel was significant. For the case of $f = 5$ Hz, the maximum stress amplitude along the inner wall increased 51%

compared with the no-fault case. When the tunnel was in the hanging wall of the fault fracture zone, $f = 10$ Hz and 20 Hz, the maximum stress amplitude along the inner wall of the tunnel decreased.

Generally speaking, the horizontal displacements of lined tunnel were greater than the vertical displacements. The reason was that the SV waves had a greater influence

(a) no fault

(b) the lined tunnel in the foot wall ($\alpha = 45°$)

(c) the lined tunnel in the hanging wall ($\alpha = 45°$)
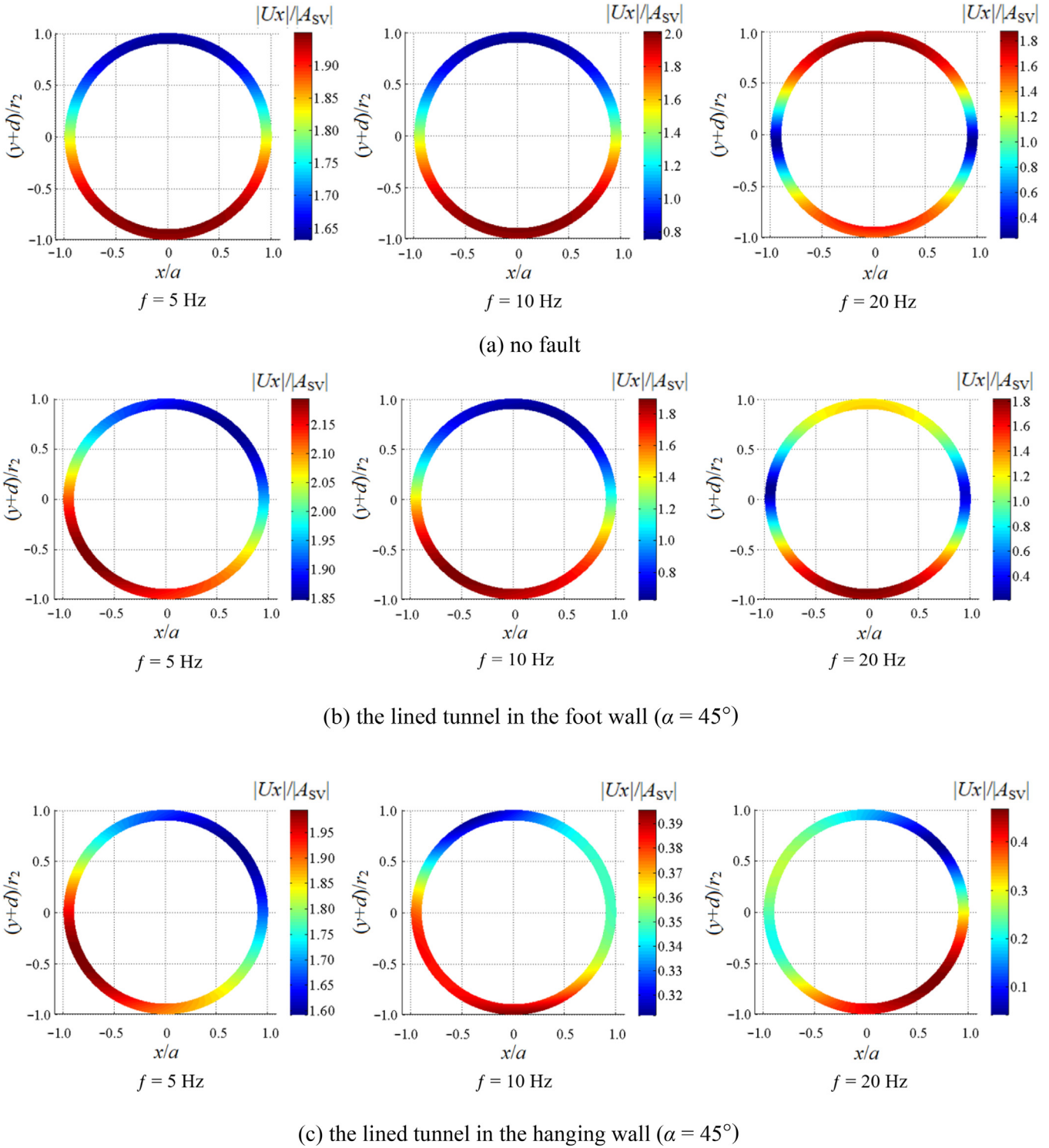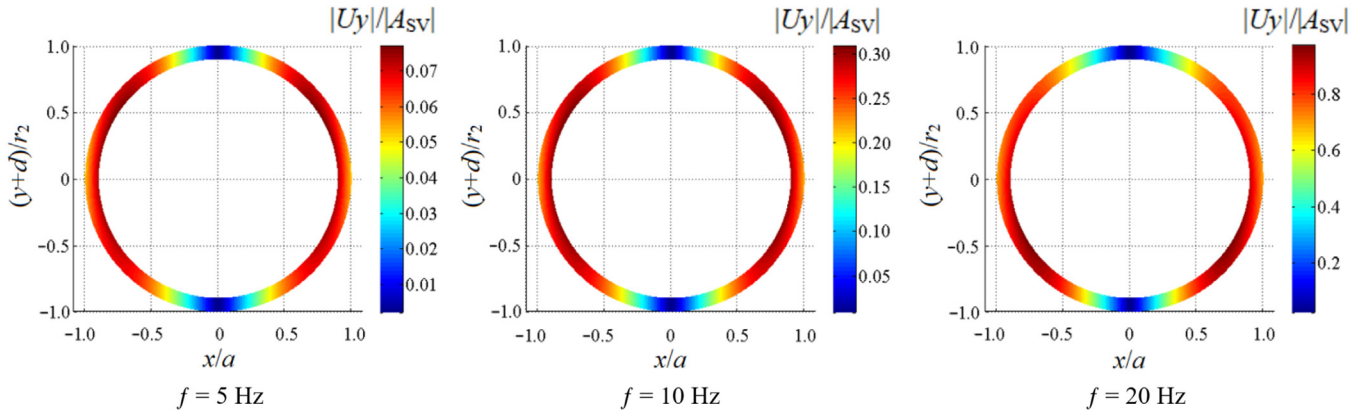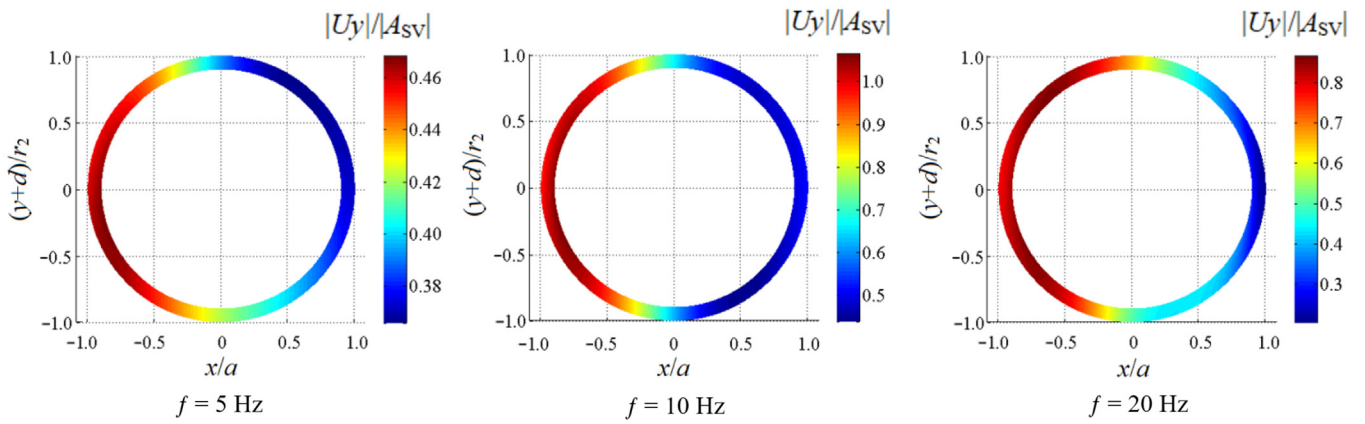
Fig. 11. Horizontal displacement cloud diagrams of the lined tunnel in a near fault site.

on horizontal displacements than vertical displacements. With the increase of frequency, the spatial distribution of displacement in the tunnel was more complicated. When
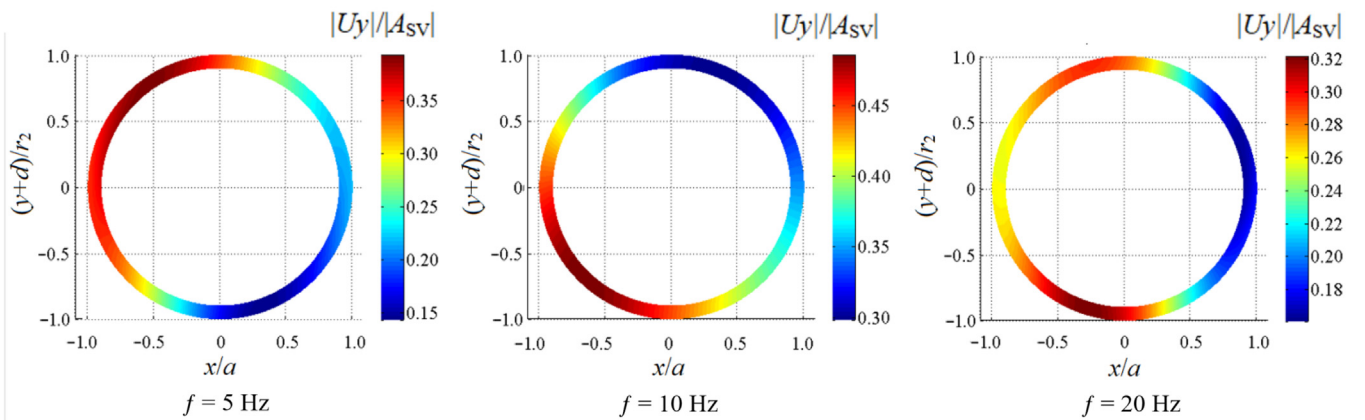
the tunnel was in the foot wall of the fault fracture zone, the horizontal and vertical displacements increased in comparison with that without fault. When the tunnel was in the

(a) no fault

(b) the lined tunnel in the foot wall ($\alpha = 45°$)

(c) the lined tunnel in the hanging wall ($\alpha = 45°$)

Fig. 12. Vertical displacement cloud diagrams of the lined tunnel in a near fault site.

hanging wall of the fault fracture zone, the horizontal and vertical displacements were reduced compared with that without fault. The horizontal displacement of high frequency wave decreased obviously. It could be seen from Fig. 11 that for the case of $\alpha = 45°$, $S = 50$ m, $f = 10$ Hz, the peak value of horizontal displacement decreased 78%.

6 Conclusions

The non-causative fault fracture zone had a significant impact on the seismic response of the underground lined tunnel. The rule of influence could be summarized from the incident frequency of the incident waves, the fault fracture zone dip angle, the distance between the tunnel, and the fault fracture zone. The IBEM was used to study the overall seismic response of the fault-tunnel (rigid) and the stress cloud picture was simulated. Comparing the interaction between the fault fracture zone and the lined tunnel when the tunnel was in the hanging or foot wall of the fault, several important conclusions could be obtained:

(1) There was an obvious seismic interaction between the fault fracture zone and the lined tunnel. The fault fracture zone had a tremendous effect on the soil layer around the lined tunnel, which caused the ground motion to be spatially redistributed. According to different parameter conditions, the seismic damage of the lined tunnel had different changes.

(2) It is worth noting that the hoop stress on the inner surface of the tunnels embedded in the fault area was significantly greater than that on the outer surface. Therefore, in practical engineering, the inner walls of tunnels near fault area should be strengthened.

(3) When the lined tunnel was in the foot wall of the fault fracture zone, the stress amplification effect of the lined tunnel increased with the increase of the inclination of the fault with an amplification factor of up to 117%. Therefore, seismic fortification should be strengthened for buried tunnels in a fault fracture zone of great inclination.

(4) For the lined tunnel structure during the ground motion near fault site, the extreme value of stress generally appeared at the arch shoulders and the arch feet, while the top and the bottom were relatively safe.

Declaration of Competing Interest

The authors declare that they have no known competing financial interests or personal relationships that could have appeared to influence the work reported in this paper.

Acknowledgments

References

Alielahi, H., & Adampira, M. (2018). Evaluation of 2D seismic site response due to hill-cavity interaction using boundary element technique. *Journal of Earthquake Engineering, 22*(6), 1137–1167.

Alielahi, H., Kamalian, M., & Adampira, M. (2015). Seismic ground amplification by unlined tunnels subjected to vertically propagating SV and P waves using BEM. *Soil Dynamics and Earthquake Engineering, 71*, 63–79.

Ardeshiri-Lajimi, S., Yazdani, M., & Langroudi, A. A. (2015). Control of fault lay-out on seismic design of large underground caverns. *Tunnelling and Underground Space Technology, 50*, 305–316.

Cai, M. (2008). Influence of stress path on tunnel excavation response - Numerical tool selection and modeling strategy. *Tunnelling and Underground Space Technology, 23*(6), 618–628.

Cividini, A., Gioda, G., & Petrini, V. (2010). Finite element evaluation of the effects of faulting on a shallow tunnel in alluvial soil. *Acta Geotechnica, 5*(2), 113–120.

Fan, L. F., Wang, L. J., & Wu, Z. J. (2018). Wave transmission across linearly jointed complex rock masses. *International Journal of Rock Mechanics and Mining Sciences, 112*, 193–200.

Fan, L. F., Wang, L. J., Wang, M., & Wu, Z. J. (2020). Investigation of stress wave transmission across a nonlinearly jointed complex rock mass. *International Journal of Rock Mechanics and Mining Sciences, 136*, 104485.

Gao, Y., Dai, D., Zhang, N., Wu, Y., & Mahfouz, A. H. (2017). Scattering of plane and cylindrical sh waves by a horseshoe shaped cavity. *Journal of Earthquake and Tsunami, 11*(2), 1650011.

Gharti, H. N., Oye, V., Komatitsch, D., & Tromp, J. (2012). Simulation of multistage excavation based on a 3D spectral-element method. *Computers & Structures, 100*(101), 54–69.

Huang, J., Zhao, M., & Du, X. (2017). Non-linear seismic responses of tunnels within normal fault ground under obliquely incident P waves. *Tunnelling and Underground Space Technology, 61*, 26–39.

Karabulut, H., & Bouchon, M. (2007). Spatial variability and non-linearity of strong ground motion near a fault. *Geophysical Journal International, 170*(1), 262–274.

Lambrecht, L., & Friederich, W. (2010). 3D simulation of seismic wave propagation around a tunnel using the spectral element method. In EGU General Assembly Conference Abstracts, 2010EGUGA.12.8632L.

Lee, V. W., & Trifunac, M. D. (1979). Response of tunnels to incident SH-waves. *Journal of the Engineering Mechanics Division, 105*(4), 643–659.

Li, T. B. (2008). Failure characters and influence factor analysis of hill tunnels at epicenter zones of great Wenchuan earthquake. *Journal of Engineering Geology, 16*(6), 742–750, in Chinese.

Li, T. C., Yin, Y. T., & Liu, J. Z. (2012). Analysis on seismic damage mechanism and anti-seismic measures of tunnels in fault fracture zone. *Advanced Materials Research, 446*, 2110–2117.

Liang, J., Luo, H., & Lee, V. W. (2010). Diffraction of plane SH waves by a semi-circular cavity in half-space. *Earthquake Science, 23*(1), 5–12.

Liang, J. W., Feng, L. X., & Ba, Z. N. (2009). Scattering of plane SV waves by local fault site. *Journal of Natural Disasters, 18*(5), 94–106, in Chinese.

Liang, J. W., Zhang, H., & Lee, V. W. (2004). A series solution for surface motion amplification due to underground group cavities: Incident P waves. *Acta Seismologica Sinica, 17*(3), 296–307.

Lin, K., Hung, H., Yang, J. P., & Yang, Y. (2016). Seismic analysis of underground tunnels by the 2.5 D finite/infinite element approach. *Soil Dynamics and Earthquake Engineering, 85*, 31–43.

Lin, M. L., Jeng, F. S., Huang, T. H., Chung, C. F., & Lee, H. H. (2006). A study on the damage degree of shield tunnels submerged in overburden soil during the thrust fault offset. In Proceedings of the ASME 2006 Pressure Vessels and Piping/ICPVT-11 Conference, July 23 July 23–27, 2006, Vancouver, BC, Canada (pp. 27–33).

Liu, Q., & Wang, R. (2012). Dynamic response of twin closely-spaced circular tunnels to harmonic plane waves in a full space. *Tunnelling and Underground Space Technology, 32*, 212–220.

Liu, Z., Ju, X., Wu, C., & Liang, J. (2017). Scattering of plane P1 waves and dynamic stress concentration by a lined tunnel in a fluid-saturated

poroelastic half-space. *Tunnelling and Underground Space Technology, 67*, 71–84.

Manolis, G. D., Parvanova, S. L., Makra, K., & Dineva, P. S. (2015). Seismic response of buried metro tunnels by a hybrid FDM-BEM approach. *Bulletin of Earthquake Engineering, 13*(7), 1953–1977.

Panji, M., & Ansari, B. (2017). Transient SH-wave scattering by the lined tunnels embedded in an elastic half-plane. *Engineering Analysis with Boundary Elements, 84*, 220–230.

Parvanova, S. L., Dineva, P. S., Manolis, G. D., & Wuttke, F. (2014). Seismic response of lined tunnels in the half-plane with surface topography. *Bulletin of Earthquake Engineering, 12*(2), 981–1005.

Pitilakis, K., Tsinidis, G., Leanza, A., & Maugeri, M. (2014). Seismic behaviour of circular tunnels accounting for above ground structures interaction effects. *Soil Dynamics and Earthquake Engineering, 67*, 1–15.

Rodriguez-Castellanos, A., Sánchez-Sesma, F. J., Luzon, F., & Martin, R. (2006). Multiple scattering of elastic waves by subsurface fractures and cavities. *Bulletin of the Seismological Society of America, 96*(4A), 1359–1374.

Shahrour, I., Khoshnoudian, F., Sadek, M., & Mroueh, H. (2010). Elastoplastic analysis of the seismic response of tunnels in soft soils. *Tunnelling and Underground Space Technology, 25*(4), 478–482.

Stamos, A., & Beskos, D. (1996). 3-D seismic response analysis of long lined tunnels in half-space. *Soil Dynamics and Earthquake Engineering, 15*(2), 111–118.

Wang, L. S., Wang, Z. H., & Kong, H. (2014). Seismic response analysis of the fault fracture zones with saturated soil under incident SV waves. *Applied Mechanics and Materials, 638*(639/640), 1863–1868.

Wang, Q., Chen, G., & Guo, E. D. (2012). Analysis on characters of cross-fault tunnel under action of earthquake. *Mechanics and Materials, 166/167/168/169*, 2016–2019.

Wang, W., Wang, T., Su, J., Lin, C., Seng, C., & Huang, T. (2001). Assessment of damage in mountain tunnels due to the Taiwan Chi-Chi earthquake. *Tunnelling and Underground Space Technology, 16*(3), 133–150.

Yu, H., Yuan, Y., & Bobet, A. (2017). Seismic analysis of long tunnels: A review of simplified and unified methods. *Underground Space, 2*(2), 73–87.

Yu, H., Zhang, Z., Chen, J., Bobet, A., Zhao, M., & Yuan, Y. (2018). Analytical solution for longitudinal seismic response of tunnel liners with sharp stiffness transition. *Tunnelling and Underground Space Technology, 77*, 103–114.

Zhang, L., & Liu, Y. (2020). Numerical investigations on the seismic response of a subway tunnel embedded in spatially random clays. *Underground Space, 5*(1), 43–52.

Zhou, X., Fan, L., & Wu, Z. (2017). Effects of microfracture on wave propagation through rock mass. *International Journal of Geomechanics, 17*(9), 04017072.